Materials Transactions, Vol. 60, No. 6 (2019) pp. 1051 to 1060

High-Temperature Thermoelectric Properties of $Pr_{1-x}Sr_xFeO_3$ ($0.1 \leq x \leq 0.7$)*1

Hiroshi Nakatsugawa[1,*2], Miwa Saito[2] and Yoichi Okamoto[3]

[1]*Yokohama National University, Yokohama 240-8501, Japan*
[2]*Kanagawa University, Yokohama 221-8686, Japan*
[3]*National Defense Academy, Yokosuka 239-8686, Japan*

Polycrystalline specimens of $Pr_{1-x}Sr_xFeO_3$ ($0.1 \leq x \leq 0.7$) were synthesized using a solid state reaction method. All samples had a typical perovskite structure, where the orthorhombic (*Pbnm*) phase was dominant at $x \leq 0.5$ and the rhombohedral (*R*-3*c*) phase was dominant at $x \geq 0.6$. Since the B site is in the mixed valence state of Fe^{3+}/Fe^{4+} and the spin quantum number is in the range of $0.86 \leq s \leq 1.15$, it is expected that Fe^{3+} is in the spin state of low spin (LS) Fe^{3+} or intermediate spin (IS) Fe^{3+} and Fe^{4+} is in the spin state of LS Fe^{4+}. As x increases, the ratio of IS Fe^{3+} decreases compared to that of LS Fe^{3+} at $x \geq 0.3$, so that the P-type Seebeck coefficient is maintained up to $x = 0.5$. Although $ZT = 0.002$ ($T = 850$ K) of $x = 0.7$ which shows the maximum N-type thermoelectric characteristic is about 8% of $ZT = 0.024$ ($T = 850$ K) of $x = 0.1$ which shows the maximum P-type thermoelectric characteristic, both are the results of relatively high Seebeck coefficient, low electrical resistivity, and low thermal conductivity. Therefore, we strongly suggest that there is a possibility of application of PN elements which compose of the perovskite-type oxides. [doi:10.2320/matertrans.E-M2019812]

(Received November 23, 2018; Accepted January 29, 2019; Published April 5, 2019)

Keywords: *thermoelectric properties, perovskite structure, spin state, Heikes formula, ZT value*

1. Introduction

Thermoelectric conversion materials are expected to be applied as energy harvesting, which directly converts unutilized waste heat discharged from power plants and automobiles to electric energy for effective utilization, and the researches targeting various materials are vigorously pursued. In particular, thermoelectric conversion materials used for recovering electric energy from high-temperature waste heat are required to be chemically stable for a long period of time in a high-temperature atmosphere. At the same time, it is also expected to be a thermoelectric conversion material in recent years. Furthermore, it is required to be a material which is abundant as a resource and composed of elements having relatively low toxicity. From the above point of view, it is an extremely attractive material as a candidate for thermoelectric conversion materials supporting a future sustainable society.

Oxide material has attracted attention as a candidate for thermoelectric conversion material with $NaCo_2O_4$ discovered by Terasaki *et al.*[1)] in 1997. The reason why $NaCo_2O_4$ shows high P-type thermoelectric characteristics ($\rho = 2\,\mu\Omega\,m$ and $S = 100\,\mu V\,K^{-1}$ at room temperature) is due to the fact that a correlated electron system[2)] because of the high density of state near the Fermi energy in the narrow bandwidth of the Co t_{2g} band shows the large Seebeck coefficient S which is one order of magnitude larger than that of general metals in spite of a high carrier density (about $10^{27}\,m^{-3}$) as metal. Then, as the oxide thermoelectric conversion material exhibiting P-type thermoelectric characteristics, a series of misfit layered Co oxides represented by $Ca_3Co_4O_9$ was reported.[3–14)] On the other hand, Al-doped ZnO[15–17)] which is a wide gap degenerate semiconductor, and a partially substituted perovskite structure $CaMnO_3$[18,19)] which is a strongly correlated electron system is known for the oxide thermoelectric conversion material exhibiting N-type thermoelectric characteristics. In fact, Urata *et al.*[20)] made the oxide thermoelectric module using $Ca_{2.7}Bi_{0.3}Co_4O_9$ for P-type and $CaMn_{0.98}Mo_{0.02}O_3$ for N-type, and estimated the maximum energy conversion efficiency of 2.0%. Furthermore, it is also reported that the N-type element breaks due to the difference in thermal expansion coefficient between PN elements. Urata *et al.*[20)] has reported the linear expansion coefficient of P-type and N-type elements to be 8 to $9\,\mu K^{-1}$ and 11 to $13\,\mu K^{-1}$, respectively in the temperature range from 373 K to 1173 K. Nagasawa *et al.*[21)] also reported the coefficient of linear expansion of the P-type element to be 9 to $10\,\mu K^{-1}$ in the same temperature range.

Among oxides having a perovskite structure, Nb-doped $SrTiO_3$,[22)] $Ca_{1-x}A_xMnO_3$ (A = Yb, Tb, Nd, Ho),[23)] $La_{1-x}Sr_xFeO_3$,[24)] $La_{1-x}Sr_xCoO_3$[25)] and so on are reported as oxides which show relatively large Seebeck coefficient S. These large S is considered to be the result of strong interaction of the spin state, orbital, charge, and crystal structure of the 3d transition metal element. Koshibae *et al.*[26)] extended the Heikes' formula to a strongly correlated electron system and formulated the high-temperature limit equation of the Seebeck coefficient of 3d transition metal oxide as shown in

$$S_\infty \cong -\frac{k_B}{e}\ln\left(\frac{g_3}{g_4}\frac{x}{1-x}\right), \quad (1)$$

where k_B is the Boltzmann constant, e is the elementary charge, g_3 and g_4 are the spin and the orbital degrees of freedom of 3d electrons in trivalent and tetravalent transition metal ions, respectively, and x is the concentration of the tetravalent transition metal ion. If the difference between g_3 and g_4 is large, it is expected to be large S_∞ from the formula (1). Therefore, it is expected that the thermoelectric properties of 3d transition metal oxide can be controlled by controlling the spin state of 3d electrons in the transition metal ions. Then, we focused attention on Mn oxide with perovskite structure showing P and N-type thermoelectric characteristics. We searched for oxides having perovskite

*1This Paper was Originally Published in Japanese in J. Thermoelec. Soc. Jpn. **15** (2018) 3–13.

*2Corresponding author, E-mail: naka@ynu.ac.jp

structure that exhibit thermoelectric properties of P-type comparable to partially substituted $CaMnO_3$[18,19,25] showing thermoelectric properties of N-type, and found that $Pr_{0.9}Sr_{0.1}MnO_3$ shows $ZT = 0.0035$ at 468 K which is the P-type thermoelectric characteristics.[27] Furthermore, we obtained that $Pr_{0.9}Sr_{0.1}FeO_3$ also shows $ZT = 0.024$ at $T =$ 850 K which is the P-type thermoelectric characteristics.[28]

Although it was revealed that Fe-oxide exhibits higher P-type thermoelectric characteristics than Mn-oxide, the correlation between the spin state of Fe ions and the thermoelectric property of Fe-oxide has not yet been clarified. Applying eq. (1) on the assumption that the spin state of Fe ion is in the mixed valence state with low spin $Fe^{3+}(t_{2g}{}^5)$; $g_3 = 6$ and low spin $Fe^{4+}(t_{2g}{}^4)$; $g_4 = 9$, the high-temperature limit of Seebeck coefficients are expected to be $S_\infty \cong 224\,\mu V\,K^{-1}$ for $x = 0.1$ and $S_\infty \cong -38\,\mu V\,K^{-1}$ for $x = 0.7$. On the other hand, the assumption that the spin state of Fe ion is the mixed valence state with intermediate spin $Fe^{3+}(t_{2g}{}^4e_g{}^1)$; $g_3 = 24$ and low spin $Fe^{4+}(t_{2g}{}^4)$; $g_4 = 9$, the high-temperature limit of Seebeck coefficients are expected to be $S_\infty \cong 105\,\mu V\,K^{-1}$ for $x = 0.1$ and $S_\infty \cong -158\,\mu V\,K^{-1}$ for $x = 0.7$. Thus, if we can realize the low spin state of Fe^{3+} or Fe^{4+} by partially replacing Sr^{2+} having a smaller ionic radius than Pr^{3+} and releasing the chemical pressure applied to Fe ions by precisely controlling the Fe–O distance and the Fe–O–Fe angle, it is possible to construct a PN element with high thermoelectric characteristics only using the Fe-oxides having the perovskite structure. In this study, the polycrystalline sample of $Pr_{1-x}Sr_xFeO_3$ ($0.1 \leq x \leq 0.7$) was prepared, and the correlation between the crystal structure, the magnetic properties and the thermoelectric characteristics was clarified by considering the spin state of Fe ions. However, $Pr_{1-x}Sr_xFeO_3$ ($0.1 \leq x \leq 0.7$) avoiding the Sr-rich sample was prepared, the thermoelectric characteristics of P-type and N-type were evaluated and the maximum value of ZT was revealed because $SrFeO_3$ is easy to take oxygen deficient composition and is required oxygen atmosphere above 500 atm for synthesis.[29–31] Furthermore, applying eq. (1) to the spin states of Fe^{3+} and Fe^{4+} obtained from the magnetic properties, we estimated S_∞ and compared it with the high-temperature limit of the Seebeck coefficient. Finally, we determined the spin states of Fe ions.

2. Experimental

Polycrystalline specimens of $Pr_{1-x}Sr_xFeO_3$ ($0.1 \leq x \leq 0.7$) were synthesized using a general solid reaction method. The compounds starting from stoichiometric mixtures 5 g of Pr_6O_{11} (99.9%, 3 N, Wako Pure Chemical Industries, Ltd.), $SrCO_3$ (99.99%, 4 N, Wako Pure Chemical Industries, Ltd.), Fe_2O_3 (99.9%, 3 N, Wako Pure Chemical Industries, Ltd.) in an agate mortar with ethanol 20 ml for 1 h were calcinated at 1273 K for 24 h in air. The calcined powder samples were pressed into pellets under a pressure of 16 MPa and sintered for 48 h in an oxygen atmosphere at 1573 K. X-ray diffraction (XRD) data were measured using a diffractometer (RINT 2500, Rigaku Corporation) using a CuKα ($\lambda = 1.542$ Å) radiation with a pyrolytic graphite monochromator at room temperature. Crystal structure parameters were refined by the Rietveld analysis using the RIETAN-FP program[32] with XRD data in a 2θ range from 10° to 90° in a scanning step of 0.02°. The microstructures of the samples were observed using a scanning electron microscope (VE-8800, KEYENCE).

The magnetic susceptibility with increasing temperature was measured in the temperature range from 5 K to 700 K using a direct-current type superconducting quantum interference device (SQUID) magnetometer (MPMS, Quantum Design, Inc.) under zero magnetic field cooling (ZFC) condition at a magnetic field of 1 T in a warming process. The electric resistivity ρ was measured by a direct-current four-probe method in a temperature range from room temperature to 850 K using a homemade apparatus. The Seebeck coefficient S was measured using a steady-state technique in a temperature range from 80 K to room temperature by the ResiTest8300 apparatus (TOYO Co.), and in the temperature range from room temperature to 850 K by the homemade apparatus. Thermal conductivity κ was calculated using the relationship of $\kappa = d\alpha C_V$ with a bulk density d, a thermal diffusivity α, and a specific heat C_V. The bulk density d was measured at room temperature by the Archimedes method using a specific gravity measurement kit (SMK-401, SHIMADZU Co.), and the relative density of all samples was measured in the range from 86% to 97%. The specific heat C_V was measured in a temperature range from room temperature to 323 K using a differential scanning calorimetry using an X-DSC 7000 apparatus (Hitachi High-Tech Science Co.). In addition, the thermal diffusivity α was measured with a temperature range from room temperature to 973 K using the laser flash method (TC-7000, ULVAC-RIKO Co.).

3. Results and Discussion

The XRD pattern of the polycrystalline samples $Pr_{1-x}Sr_xFeO_3$ ($0.1 \leq x \leq 0.7$) at room temperature are shown in Fig. 1. All the samples have a typical single-phase perovskite structure at room temperature, but it was thought that the change of crystal structure at 850 K or less does not have a big influence on physical properties. The crystal structure analysis was carried out using an orthorhombic structure (*Pbnm*) for $x \leq 0.5$ and a rhombohedral structure (R-3c) for $x \geq 0.6$. The crystal structure parameters refined by the Rietveld analysis using the RIETAN-FP program[32] are summarized in Table 1. In this study, the isotropic atomic displacement parameters B in the analysis were fixed to 0.5 Å^2 for the cation and to 1.0 Å^2 for the oxygen ions, and a split pseudo-Voigt function was used to fit the Bragg peak shapes for the Rietveld analysis. The reliability factor of the weighted diffraction pattern R_{wp} is $10\% < R_{wp} < 15\%$ at $0.1 \leq x \leq 0.7$, and the index $S = R_{wp}/R_e$ indicating a comparison with R_e corresponding to the statistically expected minimum R_{wp} is $1.4 < S < 2.2$. Thus, it is judged that some good fitting has been obtained. Furthermore, Fe–O1 and Fe–O2 distances, Fe–O1–Fe and Fe–O2–Fe angles, Goldschmidt tolerance factor[33] indicating the degree of distortion of the octahedral $FeO1_2O2_4$ of the perovskite ABO_3 structure, and the bond valence sum (BVS)[34] showing the valence of cations in the A and B sites are summarized in Table 1, where O1 is the oxygen in the principal axis

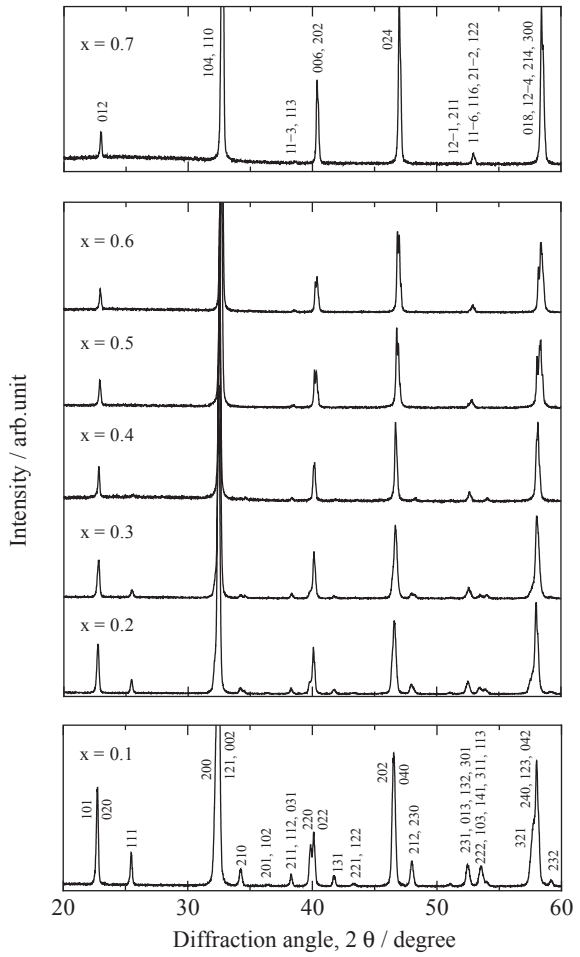

Fig. 1 X-ray diffraction patterns of $Pr_{1-x}Sr_xFeO_3$ ($0.1 \le x \le 0.7$) at room temperature.

direction of the orthorhombic system and O2 is the direction perpendicular to the principal axis of the orthorhombic system. The Goldschmidt tolerance factor of the perovskite ABO_3 structure is defined as $(r_A + r_O)/\sqrt{2}(r_B + r_O)$, where r_A, r_B, r_O are the average ion radius of the cations of the A and B sites and the oxygen ions, respectively. Furthermore, BVS indicating the valence of the cations is defined as $\sum_j \exp[(r_0 - r_{ij})/0.37\,\text{Å}]$, where r_0 is the bond valence parameter and r_{ij} is the interionic distance between the i-th cation and the j-th oxygen ion. Here, r_0 of Pr^{3+}, Sr^{2+}, Fe^3, and Fe^{4+} were calculated using 2.138 Å, 2.118 Å, 1.750 Å, and 1.765 Å, respectively. As shown in Table 1, as x increases, the average ion radius of the A site increases and the average ion radius of B site decreases, so that the Goldschmidt tolerance factor increases and approaches 1 which is an ideal perovskite ABO_3 structure. This strongly suggests that the octahedral distortion is relaxed with increasing x. On the other hand, as x increases, the BVS at the A site decreases from 2.89 to 2.41 and the BVS at the B site increases from 3.13 to 3.73, so that a part of Fe^{3+} is oxidized to Fe^{4+} as Pr^{3+} is partially substituted with Sr^{2+}, which suggests that the cations at the B site are in a mixed valence state of Fe^{3+}/Fe^{4+}. The x dependency on Fe–O1 and Fe–O2 distances are shown in Fig. 2(a) and the x dependency on Fe–O1–Fe and Fe–O2–Fe angles are shown in Fig. 2(b). As x increases, the Fe–O1 distance and the Fe–O2 distance tend to decrease and the Fe–O1–Fe and Fe–O2–Fe angles tend to increase, but the FeO_6 octahedron is most distorted at $x = 0.3$. On the other hand, in the rhombohedral phase ($x \ge 0.6$), it is understood that the FeO_6 octahedron is isotropic, the Fe–O–Fe angle approaches 180°, and the Fe–O–Fe is linearly arranged. Since this Fe–O–Fe distance corresponds to the hopping distance a_0 of the small polaron, twice the average value of Fe–O1 and Fe–O2 distances for $x \le 0.5$, and twice the Fe–O1 distance for $x \ge 0.6$ are defined as a_0 of each sample. The X-ray Rietveld analysis pattern of $x = 0.1$ and 0.7 and the crystal structure of both samples are shown in Fig. 3(a) and 3(b), respectively. Both of them show good Rietveld analysis results of $S = R_{wp}/R_e \sim 1.7$. SEM images of $x = 0.4$ and 0.7 are shown in Fig. 4(a) and 4(b), respectively. A crystal grain size of about 50 μm is confirmed at $x = 0.7$, whereas the crystal grain size of about 5 μm is confirmed at $x = 0.4$, so that coarsening of the crystal grains due to the increase of x is confirmed. This suggests an increasing tendency of the electrical and the thermal conductivity with increasing x.

Figure 5 shows the temperature dependence of the magnetic susceptibility $\chi - \chi_0$ for the polycrystalline sample of $Pr_{1-x}Sr_xFeO_3$ ($0.1 \le x \le 0.7$) measured in the temperature range from 5 K to 700 K under ZFC condition at a magnetic field of 1 T in a warming process, where χ_0 is the contribution of temperature-independent magnetic susceptibility. In all specimens, on the high-temperature side, the decreasing tendency of $\chi - \chi_0$ is shown with increasing x, and the paramagnetism is confirmed. As shown in the inset of Fig. 5, χ_0 is estimated from the magnetic susceptibility value extrapolated at the high-temperature limit from the relation of magnetic susceptibility χ and the inverse of temperature T^{-1}. Furthermore, the temperature dependence of $(\chi - \chi_0)^{-1}$ is shown in Fig. 6. Here, the solid line shows the linear relationship with the slope for the reciprocal of the Curie constant C^{-1} in the paramagnetic region of 670 K or more. In general, the temperature dependence of paramagnetic magnetic susceptibility is inversely proportional to temperature according to $\chi = \chi_0 + C^{-1}/(T - \Theta)$, so that the reciprocal of magnetic susceptibility $(\chi - \chi_0)^{-1}$ is proportional to temperature T. Here, Θ is the Curie temperature and the effective magnetic moment μ_{eff} of the B site is defined from

$$\mu_{eff} = 2\sqrt{s(s+1)}\mu_B = \sqrt{\frac{3k_BC}{N_A}}, \qquad (2)$$

where s, μ_B, k_B, N_A are the spin quantum number of the B site, the Bohr magneton, the Boltzmann's constant, and the Avogadro's number. Thus, from C estimated from the slope of the solid line in Fig. 6, the mixed valence state of Fe^{3+}/Fe^{4+} is clarified. Table 2 summarizes χ_0 estimated from the inset of Fig. 5, Θ and C estimated from Fig. 6, and μ_{eff} and s calculated from eq. (2). In all samples, since the spin quantum number is in the range of $0.86 \le s \le 1.15$, it is expected that Fe^{3+} is in a spin state of low spin (LS) Fe^{3+} ($t_{2g}{}^5$); $s = 0.5$ or intermediate spin (IS) Fe^{3+} ($t_{2g}{}^4e_g{}^1$); $s = 1.5$ and Fe^{4+} is in a spin state of low spin (LS) Fe^{4+} ($t_{2g}{}^4$); $s = 1.0$. Therefore, assuming that the mixed valence state of Fe^{3+}/Fe^{4+} at the B site is (LS $Fe^{3+}{}_y$ IS $Fe^{3+}{}_{1-y})_{1-x}$ LS $Fe^{4+}{}_x$ ($0.1 \le x \le 0.7$), the spin quantum number is estimated

Table 1 Crystal structure parameters of $Pr_{1-x}Sr_xFeO_3$ ($0.1 \le x \le 0.7$) at room temperature.

samples		$Pr_{1-x}Sr_xFeO_3$						
composition, x		0.1	0.2	0.3	0.4	0.5	0.6	0.7
space group		*Pbnm*	*Pbnm*	*Pbnm*	*Pbnm*	*Pbnm*	*R-3c*	*R-3c*
average ionic radius of A site (Å)		1.205	1.231	1.257	1.283	1.310	1.336	1.362
average ionic radius of B site (Å)		0.639	0.633	0.627	0.621	0.615	0.609	0.603
Goldschmidt tolerance factor		0.903	0.915	0.927	0.939	0.951	0.963	0.975
BVS of A site in ABO_3: valence units (v.u.)		2.89	2.79	2.75	2.56	2.50	2.48	2.41
BVS of B site in ABO_3: valence units (v.u.)		3.13	3.18	3.30	3.47	3.56	3.68	3.73
a (Å)		5.4906(5)	5.4937(6)	5.4847(6)	5.4972(4)	5.4655(3)	5.462(1)	5.4605(7)
b (Å)		5.5462(5)	5.5499(6)	5.5348(7)	5.4799(4)	5.5008(3)	5.462(1)	5.4605(7)
c (Å)		7.7827(7)	7.7775(9)	7.7599(9)	7.7515(6)	7.7286(4)	13.361(2)	13.386(2)
V (Å^3)		237.00(3)	237.13(4)	235.56(5)	233.51(3)	232.36(2)	345.3(1)	345.69(9)
$a/\sqrt{2}$ (Å)		3.8824	3.8846	3.8783	3.8871	3.8647	3.8622	3.8612
$b/\sqrt{2}$ (Å)		3.9218	3.9244	3.9137	3.8749	3.8896	3.8622	3.8612
$c/2$ (Å) (*Pbnm*)		3.8914	3.8888	3.8800	3.8758	3.8643	—	—
Pr / Sr	x	0.0079(2)	0.0062(3)	0.0055(4)	0.002(1)	0.000(1)	0	0
	y	-0.0398(1)	-0.0396(2)	-0.0338(3)	-0.0182(3)	-0.0017(6)	0	0
	z	1/4	1/4	1/4	1/4	1/4	1/4	1/4
	B (Å^2)	0.5	0.5	0.5	0.5	0.5	0.5	0.5
	g	1.0	1.0	1.0	1.0	1.0	1.0	1.0
Fe	x	1/2	1/2	1/2	1/2	1/2	0	0
	y	0	0	0	0	0	0	0
	z	0	0	0	0	0	0	0
	B (Å^2)	0.5	0.5	0.5	0.5	0.5	0.5	0.5
	g	1.0	1.0	1.0	1.0	1.0	1.0	1.0
O1	x	-0.080(2)	-0.076(2)	-0.087(3)	-0.048(5)	-0.036(6)	0.534(1)	0.526(1)
	y	0.513(1)	0.501(2)	0.494(3)	0.497(3)	0.459(3)	0	0
	z	1/4	1/4	1/4	1/4	1/4	1/4	1/4
	B (Å^2)	1.0	1.0	1.0	1.0	1.0	1.0	1.0
	g	1.0	1.0	1.0	1.0	1.0	1.0	1.0
O2 (*Pbnm*)	x	0.711(1)	0.709(1)	0.707(1)	0.731(5)	0.748(1)	—	—
	y	0.289(1)	0.296(2)	0.276(4)	0.270(5)	0.251(9)	—	—
	z	-0.034(1)	-0.023(1)	-0.015(1)	-0.029(2)	-0.025(2)	—	—
	B (Å^2)	1.0	1.0	1.0	1.0	1.0	—	—
	g	1.0	1.0	1.0	1.0	1.0	—	—
R_{wp} (%)		11.708	14.136	15.067	10.452	11.228	13.903	10.389
R_p (%)		8.298	10.095	11.229	7.926	8.181	10.322	8.248
R_R (%)		11.142	13.591	16.621	20.982	15.343	21.094	19.376
R_e (%)		7.061	6.795	6.943	7.304	7.606	6.509	6.149
R_B (%)		4.594	3.596	5.480	6.567	4.936	5.277	7.412
R_F (%)		3.017	3.241	4.530	6.626	5.044	4.689	5.695
$S = R_{wp}/R_e$		1.658	2.080	2.170	1.431	1.476	2.136	1.690
Fe - O1 (Å)	×2 (*Pbnm*)	1.996(2)	1.989(3)	1.999(4)	1.956(4)	1.954(4)	1.9398(9)	1.9367(7)
Fe - O2 (Å)	×2 (*Pbnm*)	1.987(8)	1.96(1)	1.90(2)	1.95(3)	1.94(5)	—	—
Fe - O2 (Å)	×2 (*Pbnm*)	1.997(9)	2.01(1)	2.03(1)	1.96(3)	1.95(5)	—	—
Fe - O1 - Fe (deg.)		154.1(6)	155.6(8)	152.0(9)	164(1)	162(1)	168.7(5)	171.3(4)
Fe - O2 - Fe (deg.)	(*Pbnm*)	156.6(4)	157.8(5)	162.8(9)	163(1)	168(1)	—	—

to be $s = 1.5 - 0.5x - y + xy$. If s is estimated from eq. (2), the ratio of LS Fe^{3+} to IS Fe^{3+}, i.e., y:$1-y$ is determined from

$$y = 1.5 - \frac{s - x}{1 - x}. \quad (3)$$

Table 2 summarizes the mixed valence state of Fe^{3+}/Fe^{4+} at the B site. As x increases, the ratio of IS Fe^{3+} increases with $x = 0.2$ rather than $x = 0.1$, but y increases at $x \ge 0.3$ and IS Fe^{3+} decreases relative to LS Fe^{3+}. This strongly suggests that the number of e_g electrons in the B site tends to decrease with increasing x.

Figure 7 shows the temperature dependence of the electrical resistivity ρ of the polycrystalline sample $Pr_{1-x}Sr_xFeO_3$ ($0.1 \le x \le 0.7$) in the temperature range from room temperature to 850 K. All samples show semiconductive behavior over the entire temperature range and a decrease in electrical resistivity was confirmed with increasing x. As shown in Table 2, since the mixed-valence state of the B site at $x = 0.1$ is LS $Fe^{3+}{}_{0.43}$ IS $Fe^{3+}{}_{0.47}$ LS $Fe^{4+}{}_{0.1}$, it is expected that the P-type conduction is due to the t_{2g} hole moving between LS $Fe^{3+}(t_{2g}{}^5)$–LS $Fe^{4+}(t_{2g}{}^4)$ or the e_g hole moving between IS $Fe^{3+}(t_{2g}{}^4 e_g{}^1)$–LS $Fe^{4+}(t_{2g}{}^4)$. On the other hand, since the mixed-valence state of the B site

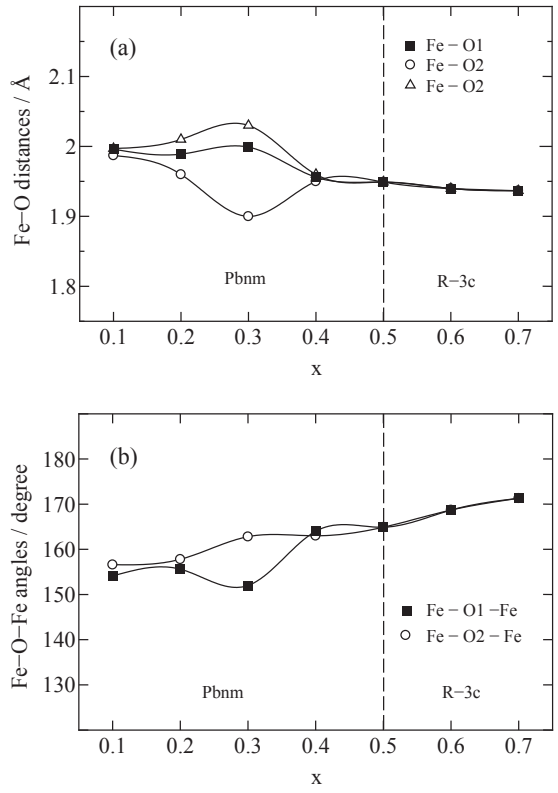

Fig. 2 Fe–O distances and Fe–O–Fe angles of $Pr_{1-x}Sr_xFeO_3$ ($0.1 \le x \le 0.7$) at room temperature.

at $x = 0.7$ is LS $Fe^{3+}{}_{0.22}$ IS $Fe^{3+}{}_{0.08}$ LS $Fe^{4+}{}_{0.7}$, it is mainly expected that the N-type conduction is due to the t_{2g} electron moving between LS $Fe^{3+}(t_{2g}{}^5)$–LS $Fe^{4+}(t_{2g}{}^4)$. As shown in Fig. 8, in addition, all samples show temperature dependence of small polaron hopping conduction at high temperature. According to Polaron theory,[35–37] the hopping conduction of the small polaron shows a thermal activation that the carrier mobility μ is more remarkable than the carrier concentration n and exhibits a temperature dependence such as $\mu \propto \exp(-W_H/k_BT)$. Here, W_H is the hopping energy of small polarons and the carrier concentration n is defined as the number of hopping of small polarons per unit volume, i.e., $n \propto \exp(-E_g/2k_BT)$, where E_g corresponds to the band gap. Therefore, the temperature dependence of the electric conductivity $\sigma = en\mu$ is expressed by

$$\sigma T = \sigma_0 \exp\left(-\frac{E_\sigma}{k_BT}\right), \quad \sigma_0 = \frac{e^2 n_0 \omega_{LO} a_0^2}{k_B},$$
$$E_\sigma = W_H + \frac{E_g}{2}, \tag{4}$$

where n_0 is the Fe^{4+} concentration per unit volume, ω_{LO} is the optical phonon frequency, a_0 is the hopping distance of the small polaron, i.e., corresponding to the Fe–O–Fe distance, and E_σ is the activation energy of the small polaron conduction.

As shown in Fig. 8, in all samples, the Arrhenius plot of σT and T^{-1} shows a linear relationship of the slope E_σ/k_B above 670 K. As summarized in Table 3, σ_0 shown in eq. (4) is obtained by extrapolating the linear relationship of σT shown in Fig. 8 to $T^{-1} \to 0$ and performing porosity correction in the range from $2.08 \times 10^7\,\Omega^{-1}\,m^{-1}\,K$ to $8.39 \times 10^7\,\Omega^{-1}\,m^{-1}\,K$. Therefore, by obtaining n_0 and a_0 from the crystal structure parameters summarized in Table 1, ω_{LO} with the porosity correction was calculated in the range from 8.4 THz to 85.2 THz (Table 3), which is consistent with typical optical phonon frequency values, i.e., $10\,THz \le \omega_{LO} \le 100\,THz$.

Figure 9 shows the temperature dependence of the Seebeck coefficient S of the polycrystalline sample $Pr_{1-x}Sr_xFeO_3$ ($0.1 \le x \le 0.7$) below 850 K. The absolute value $|S|$ of the P-type Seebeck coefficient shows a decreasing trend with increasing x, and a change to N-type Seebeck coefficient is confirmed at $x = 0.6$, showing the minimum $|S|$, whereas the N-type $|S|$ shows a slight increasing trend at $x = 0.7$. As shown in Fig. 10, in order to estimate the Seebeck coefficient at the high-temperature limit, the Seebeck coefficient S is extrapolated to $T^{-1} \to 0$ at high-temperature, and a good linear relationship is obtained for all samples above 670 K. In hopping conduction of small polaron, the T^{-1} dependence of S is given by the following equation.[38]

$$S = S_\infty \pm \frac{k_B}{e}\frac{E_S}{k_BT}, \tag{5}$$

where E_S ($\ll E_\sigma$) is the characteristic energy of the Seebeck coefficient, and S_∞ is the Seebeck coefficient at the high-temperature limit. Table 3 summarizes E_S and S_∞ for all samples. Assuming that E_S corresponds to $E_g/2$ in eq. (4), the hopping energy of the small polaron is defined as $W_H = E_\sigma - E_S$. Table 3 summarizes W_H for all samples.

If the mixed valence state of Fe^{3+}/Fe^{4+} of the B site is LS $Fe^{3+}{}_{1-x}$ LS $Fe^{4+}{}_x$ ($0.1 \le x \le 0.7$), the Seebeck coefficient at the high-temperature limit is expressed as

$$S_\infty \cong -\frac{k_B}{e}\ln\left(\frac{6}{9}\frac{x}{1-x}\right) \tag{6}$$

from eq. (1). As shown in Fig. 11, S_∞ for LS $Fe^{3+}{}_{1-x}$ LS $Fe^{4+}{}_x$ ($0.1 \le x \le 0.7$) monotonously decreases as x increases and changes from P-type to N-type at $x = 0.6$. On the other hand, if the mixed valence state of Fe^{3+}/Fe^{4+} of the B site is IS $Fe^{3+}{}_{1-x}$ LS $Fe^{4+}{}_x$ ($0.1 \le x \le 0.7$), S_∞ is expressed as

$$S_\infty \cong -\frac{k_B}{e}\ln\left(\frac{24}{9}\frac{x}{1-x}\right) \tag{7}$$

from eq. (1). As shown in Fig. 11, S_∞ for IS $Fe^{3+}{}_{1-x}$ LS $Fe^{4+}{}_x$ ($0.1 \le x \le 0.7$) also monotonously decreases as x increases and changes from P-type to N-type at $x = 0.3$. In addition, if the mixed valence state of Fe^{3+}/Fe^{4+} of the B site is (LS $Fe^{3+}{}_y$ IS $Fe^{3+}{}_{1-y})_{1-x}$ LS $Fe^{4+}{}_x$ ($0.1 \le x \le 0.7$), S_∞ is expressed as

$$S_\infty \cong -\frac{k_B}{e}\left[y\ln\left(\frac{6}{9}\frac{x}{1-x}\right) + (1-y)\ln\left(\frac{24}{9}\frac{x}{1-x}\right)\right] \tag{8}$$

from eq. (1). From the ratio of LS Fe^{3+} and IS Fe^{3+} summarized in Table 2, the result of eq. (8) is plotted in Fig. 11 with "×" marks. As shown in Fig. 11, the Seebeck coefficient at the high-temperature limit is expected to change from P-type to N-type at $x = 0.55$. Similarly, S_∞ obtained by extrapolating the straight line of eq. (5) by $T^{-1} \to 0$ (Table 3) also changed from P-type to N-type at $x = 0.58$ as shown by the dotted line plotted in Fig. 11. Therefore, the

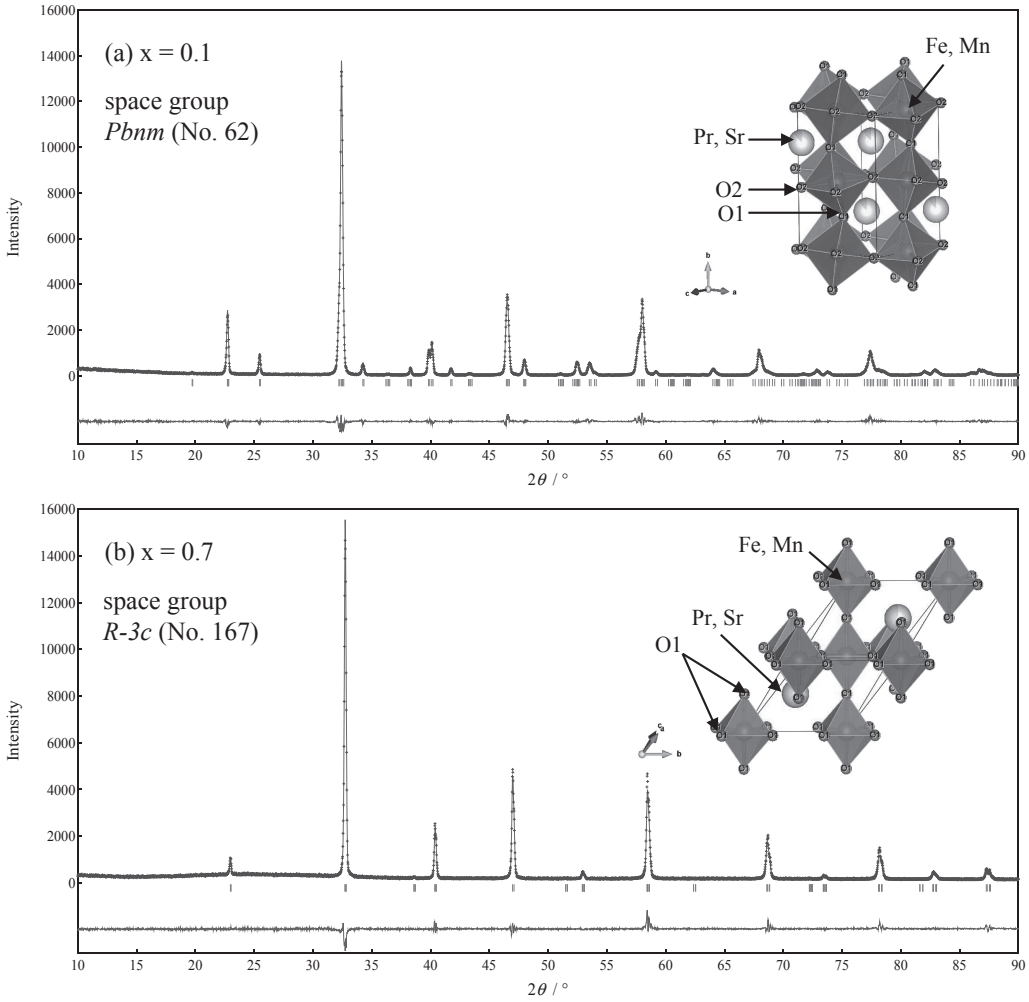

Fig. 3 X-ray Rietveld analysis patterns and crystal structures of $Pr_{1-x}Sr_xFeO_3$ ($x = 0.1$ and 0.7) at room temperature.

main factor of showing the P-type thermoelectric characteristics at $x \leq 0.5$ is that the spin state of Fe^{3+} ions in $Pr_{1-x}Sr_xFe^{3+}{}_{1-x}$ LS $Fe^{4+}{}_x$ O_3 ($0.1 \leq x \leq 0.7$) changes from the mixed state of LS Fe^{3+}/IS Fe^{3+} to the predominant state of LS Fe^{3+} with increasing x.

Figure 12 shows the temperature dependence of the power factor $S^2\sigma$ of the polycrystalline sample $Pr_{1-x}Sr_xFeO_3$ ($0.1 \leq x \leq 0.7$) calculated from Fig. 7 and Fig. 9 below 850 K. In all samples, $S^2\sigma$ monotonically increases with increasing temperature. In $0.1 \leq x \leq 0.5$ showing P-type thermoelectric characteristics, $S^2\sigma$ at $T = 850$ K shows a maximum value of 2.0×10^{-5} W m^{-1} K^{-2} at $x = 0.1$ and decreases as x increases. On the other hand, in $x \geq 0.6$ showing N-type thermoelectric characteristics, $S^2\sigma$ at $T = 850$ K shows the minimum value at $x = 0.6$ but increases to 2.8×10^{-6} W m^{-1} K^{-2} at $x = 0.7$, which is almost the same value as $x = 0.4$. Although $S^2\sigma$ ($T = 850$ K) at $x = 0.7$ shows the maximum N-type thermoelectric characteristic which is about 14% of $S^2\sigma$ ($T = 850$ K) at $x = 0.1$ showing the maximum P-type thermoelectric characteristics, this suggests that it is possible to construct a PN thermoelectric device using only perovskite Fe-oxides.

The temperature dependence of the total thermal conductivity κ ($= \kappa_L + \kappa_e$) and the electric thermal conductivity κ_e for the polycrystalline samples of $Pr_{1-x}Sr_xFeO_3$ ($0.1 \leq x \leq 0.7$) above 300 K is shown in Fig. 13. Here, κ_L is the lattice thermal conductivity and $\kappa_e = L_0\sigma T$ is calculated using well-known the Wiedemann Franz law, where $L_0 = 2.45 \times 10^{-8}$ V^2 K^{-2} is the Lorenz number. In all samples, κ_e monotonically increases with increasing temperature, but the proportion of κ_e to κ is smaller than that of κ_L to κ. In other words, in all samples, κ_L plays a more important role than κ_e, and can be regarded as $\kappa \cong \kappa_L$. Therefore, as shown in Fig. 13, in all the samples, κ maintains a relatively small value, i.e., it shows a value of about 2 W m^{-1} K^{-1} or less in the temperature range of $T \geq 300$ K.

The temperature dependence of the dimensionless figure of merit ZT for the polycrystalline samples of $Pr_{1-x}Sr_xFeO_3$ ($0.1 \leq x \leq 0.7$) at $T \leq 850$ K is shown in Fig. 14. In all the samples, ZT monotonically increases with increasing temperature. In particular, for $0.1 \leq x \leq 0.5$ indicating P-type thermoelectric characteristics, ZT at $T = 850$ K shows the maximum value of $ZT = 0.024$ at $x = 0.1$ and decreases with increasing x. On the other hand, for $x \geq 0.6$ indicating N-type thermoelectric characteristics, the ZT value is shown the minimum at $x = 0.6$, but increases to $ZT = 0.002$ at $x = 0.7$. Although ZT ($T = 850$ K) at $x = 0.7$ shows the maximum N-type thermoelectric characteristics which is about 8% of ZT ($T = 850$ K) at $x = 0.1$ showing the maximum P-type thermoelectric characteristics, both are the results of a high

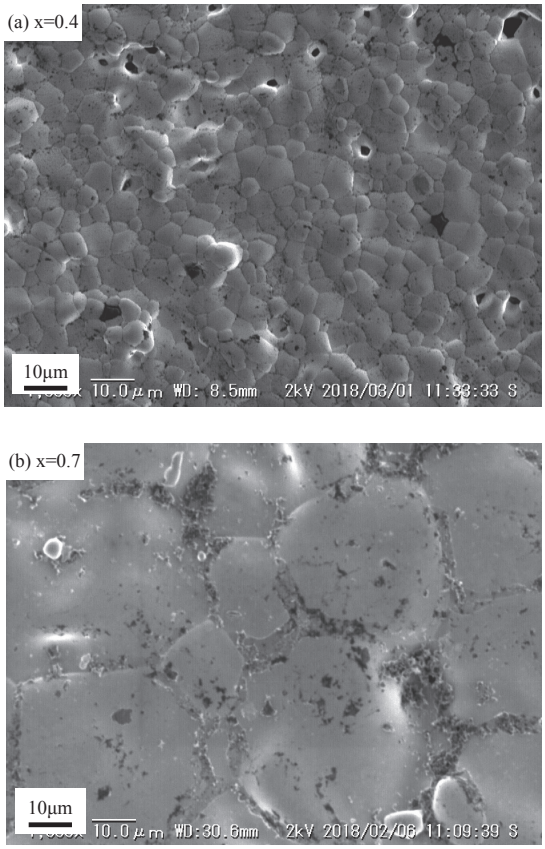

Fig. 4 SEM images of $Pr_{1-x}Sr_xFeO_3$ ($x = 0.4$ and 0.7) at room temperature.

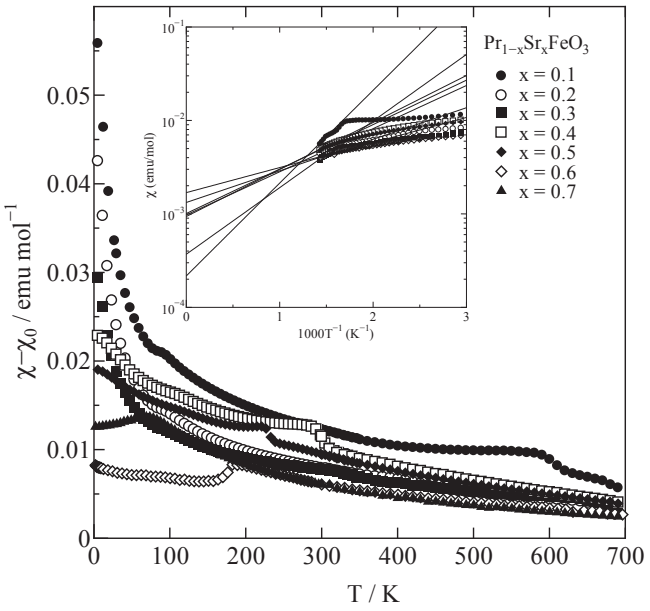

Fig. 5 Temperature dependence of magnetic dc-susceptibility ($\chi - \chi_0$) for $Pr_{1-x}Sr_xFeO_3$ ($0.1 \le x \le 0.7$) under zero-field cooling conditions at a magnetic field of 1 T during the warming process, where the temperature-independent term, χ_0, is evaluated from χ ($T \to \infty$) as shown in the inset.

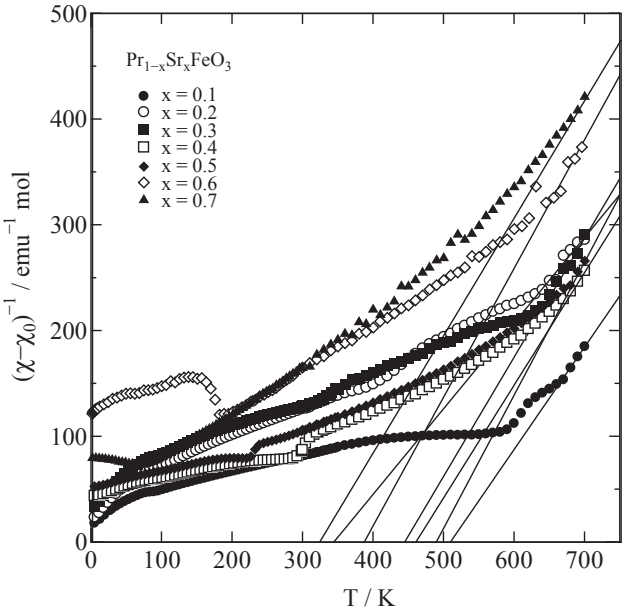

Fig. 6 Temperature dependence of inverse magnetic susceptibility $(\chi - \chi_0)^{-1}$ for $Pr_{1-x}Sr_xFeO_3$ ($0.1 \le x \le 0.7$). The straight lines represent the Curie-Weiss laws above 670 K.

Seebeck coefficient $|S|$, a relatively low electric resistivity ρ, and a low thermal conductivity κ, suggesting the possibility of constructing a PN thermoelectric device by using only perovskite Fe-oxides.

4. Conclusions

In this study, polycrystalline samples of $Pr_{1-x}Sr_xFeO_3$ ($0.1 \le x \le 0.7$) were synthesized using a conventional solid-state reaction method in order to clarify the correlation between their crystal structures, magnetic properties and thermoelectric properties. All samples had a typical single-phase perovskite structure, where the orthorhombic (*Pbnm*) phase was dominant at $x \le 0.5$, and the rhombohedral (*R*-3*c*) phase was dominant at $x \ge 0.6$. As x increases, the

Table 2 Temperature-independent magnetic susceptibilities (χ_0), paramagnetic Curie temperatures (Θ), Curie constants (C), effective magnetic moments (μ_{eff}), spin quantum number (s), ionic ratios of B-site ions for $Pr_{1-x}Sr_xFeO_3$ ($0.1 \le x \le 0.7$).

samples	$Pr_{1-x}Sr_xFeO_3$						
composition, x	0.1	0.2	0.3	0.4	0.5	0.6	0.7
χ_0 (emu mol^{-1})	0.0002	0.0010	0.0004	0.0009	0.0010	0.0013	0.0017
Θ (K)	509.9(7)	344(5)	445(3)	461(2)	489.8(3)	387(4)	322(1)
C (emu K mol^{-1})	1.032	1.235	0.888	0.938	0.794	0.821	0.901
μ_{eff} (μ_B)	2.872	3.142	2.664	2.739	2.521	2.563	2.684
spin quantum number, s	1.02	1.15	0.92	0.96	0.86	0.88	0.93
LS Fe^{3+} (s=0.5) (%)	42.9	25.1	42.7	34.2	39.4	32.5	21.8
IS Fe^{3+} (s=1.5) (%)	47.1	54.9	27.3	25.8	10.6	7.5	8.2
LS Fe^{4+} (s=1.0) (%)	10.0	20.0	30.0	40.0	50.0	60.0	70.0

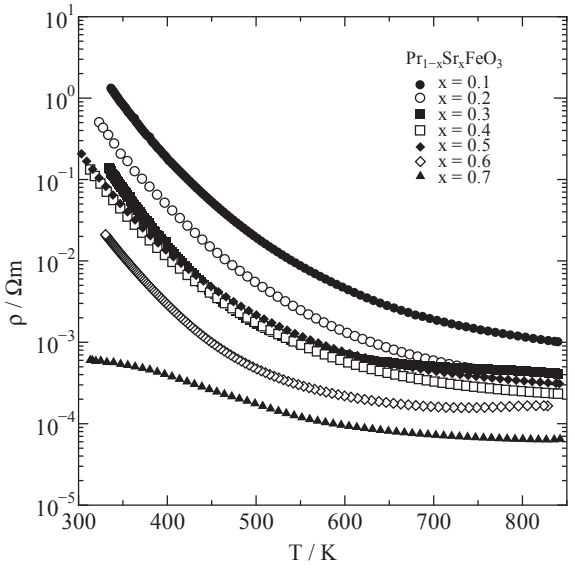

Fig. 7 Temperature dependence of electric resistivity (ρ) for $Pr_{1-x}Sr_xFeO_3$ ($0.1 \leq x \leq 0.7$).

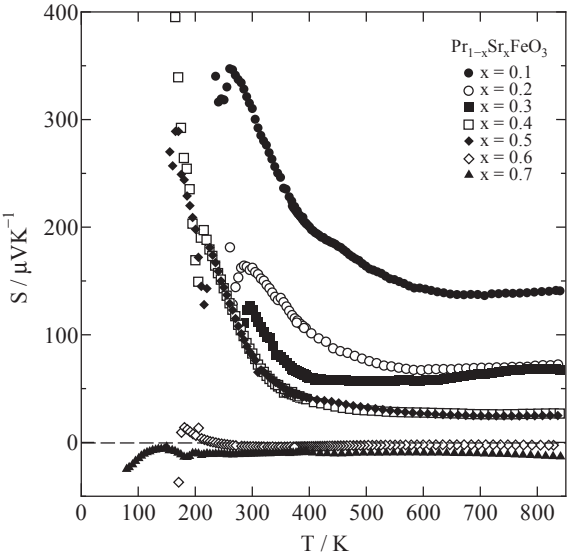

Fig. 9 Temperature dependence of Seebeck coefficient (S) for $Pr_{1-x}Sr_xFeO_3$ ($0.1 \leq x \leq 0.7$).

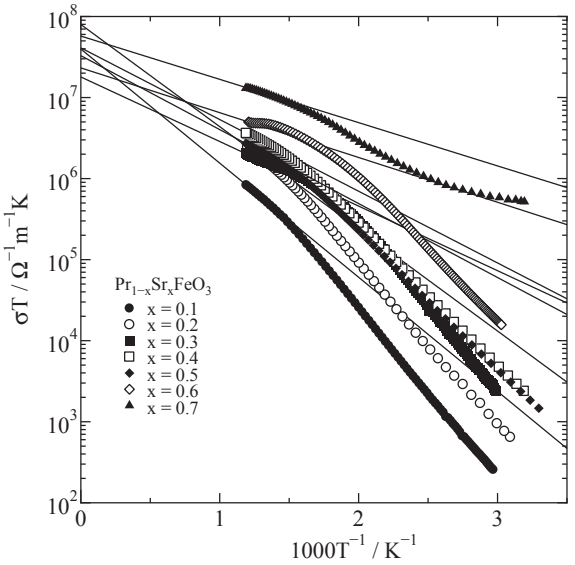

Fig. 8 Arrhenius relationship between σT and T^{-1} for $Pr_{1-x}Sr_xFeO_3$ ($0.1 \leq x \leq 0.7$), where the straight lines represent the linear portions of the Arrhenius plots.

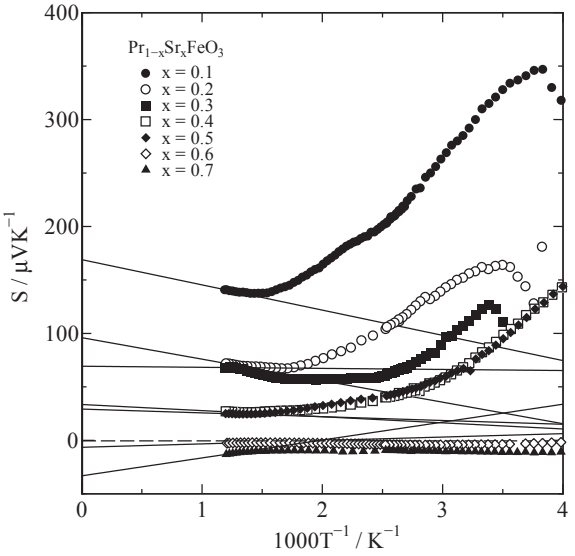

Fig. 10 Temperature dependence of Seebeck coefficient (S) for $Pr_{1-x}Sr_xFeO_3$ ($0.1 \leq x \leq 0.7$), where the straight lines represent the theoretical relationship of eq. (5).

Goldschmidt tolerance factor increases, the Fe–O1 and Fe–O2 distances tend to decrease, the Fe–O1–Fe and Fe–O2–Fe angles tend to increase, so that it is confirmed that the strain of the FeO_6 octahedron which is the maximum at $x = 0.3$ is gradually relaxed in the rhombohedral phase at $x \geq 0.6$. Also, since the B site is in the mixed valence state of Fe^{3+}/Fe^{4+} and the spin quantum number is in the range of $0.86 \leq s \leq 1.15$ in all the samples, it is expected that Fe^{3+} ions are in the spin state of LS Fe^{3+} or IS Fe^{3+} and Fe^{4+} ions are in the spin state of LS Fe^{4+}. The ratio of IS Fe^{3+} increases with $x = 0.2$ rather than $x = 0.1$, but that of IS Fe^{3+} decreases compared with LS Fe^{3+} at $x \geq 0.3$ so that it is conceivable that the e_g electrons of the B site tend to decrease with increasing x. On the other hand, all samples show the temperature dependence of small polaron hopping conduction at high-temperature, and the electrical resistivity ρ and the absolute value of the P-type Seebeck coefficient $|S|$ decreases with increasing x. Also, $|S|$ changes from P-type to N-type with increasing temperature at $x = 0.6$, and N-type $|S|$ shows a slight increase with increasing temperature at $x = 0.7$. In addition, it is suggested from the Seebeck coefficient at the high-temperature limit S_∞ that the P-type thermoelectric properties at $x \leq 0.5$ are exhibited because the spin state of Fe^{3+} ions in $Pr_{1-x}Sr_xFe^{3+}{}_{1-x}$ LS $Fe^{4+}{}_x$ O_3 changes from the mixed state of LS Fe^{3+}/IS Fe^{3+} to the predominant state of LS Fe^{3+} with increasing x. The thermal conductivity κ maintains a relatively small value in all samples, i.e., it shows a value of about 2 $Wm^{-1}K^{-1}$ or less in the temperature range of $T \geq 300$ K. Although $ZT = 0.002$ ($T = 850$ K) at $x = 0.7$ shows the maximum N-type thermoelectric proper-

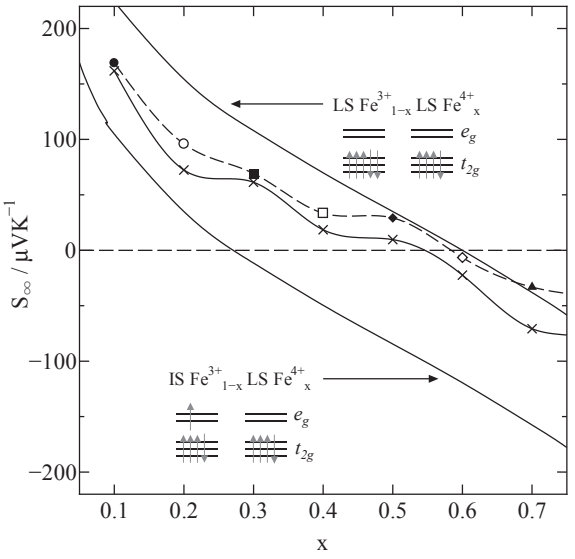

Fig. 11 Seebeck coefficient in the high-temperature limit (S_∞) for $Pr_{1-x}Sr_xFeO_3$ ($0.1 \leq x \leq 0.7$), where the solid lines represent relationships of eqs. (6), (7), and (8). On the other hand, the dotted line is evaluated from S ($T \to \infty$) as shown in Fig. 10.

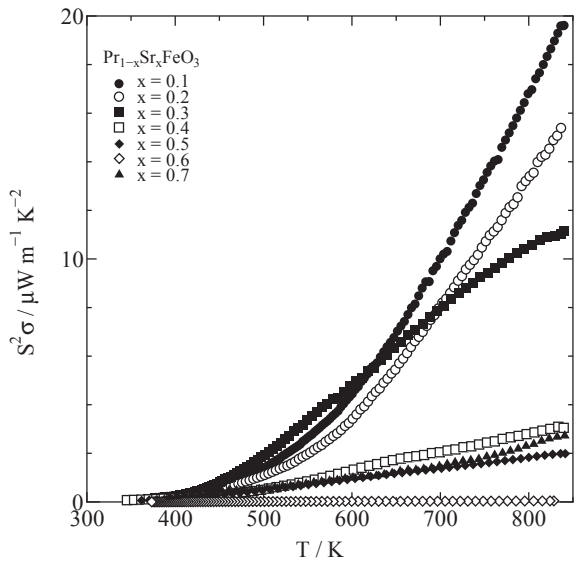

Fig. 12 Temperature dependence of power factor ($S^2\sigma$) for $Pr_{1-x}Sr_xFeO_3$ ($0.1 \leq x \leq 0.7$).

Table 3 Activation energy of electrical conduction (E_σ), pre-exponential term (σ_0), concentration of tetravalent ions per unit volume (n_0), intersite hopping distance (a_0), optical phonon frequency (ω_{LO}), characteristic energy of Seebeck coefficient (E_S), hopping energy of small polarons (W_H), Seebeck coefficient in the high-temperature limit (S_∞), S_∞ evaluated from Heikes formula, bulk density at room temperature (d), relative density at room temperature, specific heat at room temperature (C_V), thermal diffusivity at room temperature (α), and thermal conductivity at room temperature (κ) for $Pr_{1-x}Sr_xFeO_3$ ($0.1 \leq x \leq 0.7$), where $*$ means porosity-corrected physical quantity.

samples	$Pr_{1-x}Sr_xFeO_3$						
composition, x	0.1	0.2	0.3	0.4	0.5	0.6	0.7
E_σ (eV)	0.279	0.250	0.158	0.176	0.181	0.110	0.106
σ_0 ($\Omega^{-1}m^{-1}K$)	3.96×10^7	7.96×10^7	1.79×10^7	4.10×10^7	3.29×10^7	2.32×10^7	5.73×10^7
σ_0^* ($\Omega^{-1}m^{-1}K$)	4.24×10^7	8.39×10^7	2.08×10^7	4.38×10^7	3.51×10^7	2.45×10^7	5.88×10^7
n_0 (m^{-3})	1.69×10^{27}	3.37×10^{27}	5.09×10^{27}	6.85×10^{27}	8.66×10^{27}	1.04×10^{28}	1.21×10^{28}
a_0 (Å)	3.98(1)	3.97(1)	3.95(2)	3.91(4)	3.898(2)	3.879(1)	3.873(1)
ω_{LO} (THz)	79.8	80.5	12.1	21.1	13.4	7.96	16.9
ω_{LO}^* (THz)	85.2	84.8	14.1	22.5	14.4	8.41	17.3
E_S (eV)	0.024	0.020	0.001	0.006	0.004	0.003	0.017
W_H (eV)	0.256	0.230	0.157	0.170	0.177	0.106	0.089
S_∞ (μVK^{-1})	169.0(1)	96.0(1)	69.3(2)	33.5(1)	29.24(6)	−6.509(6)	−33.18(4)
d (kg m^{-3}) @RT	6278	6224	5565	5958	5864	5810	5831
relative density (%)	93.6	94.9	86.3	93.7	93.5	94.6	97.5
C_v (J kg^{-1} K^{-1}) @RT	304	316	350	362	334	370	380
α (m^2 s^{-1}) @RT	5.40×10^{-7}	7.12×10^{-7}	4.85×10^{-7}	5.62×10^{-7}	6.20×10^{-7}	4.73×10^{-7}	6.98×10^{-7}
κ (W m^{-1} K^{-1}) @RT	1.03	1.40	0.94	1.21	1.21	1.02	1.55
κ^* (W m^{-1} K^{-1}) @RT	1.10	1.48	1.09	1.29	1.29	1.08	1.59

ties which is about 8% of $ZT = 0.024$ ($T = 850$ K) at $x = 0.1$ showing the maximum P-type thermoelectric properties, both are the results of a high $|S|$, a relatively low ρ, and a low κ. Therefore, these results strongly suggest the possibility of application to high-temperature PN thermoelectric devices composed of only perovskite-type Fe-oxides of the same crystal structure.

Acknowledgments

This work was partly supported by the support of Grants-in-Aid for Scientific Research (15K06479). In addition, the magnetization measurement experiment below room temperature and observation of microstructure by

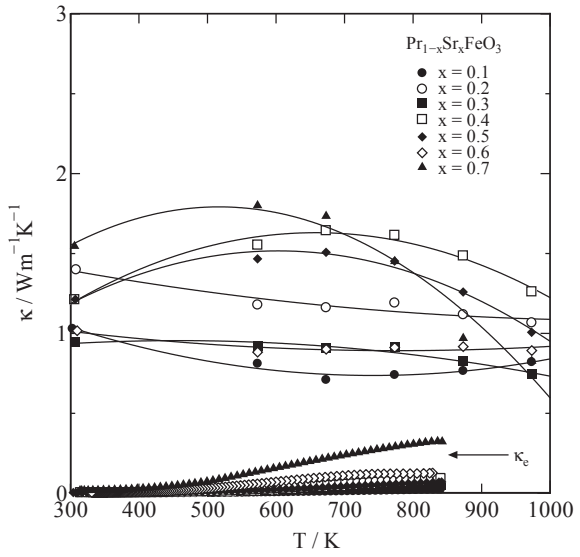

Fig. 13 Temperature dependence of the total thermal conductivity ($\kappa = \kappa_L + \kappa_e$) above room temperature for $Pr_{1-x}Sr_xFeO_3$ ($0.1 \leq x \leq 0.7$). The temperature dependence of the electric thermal conductivity ($\kappa_e = L_0\sigma T$) for all samples are also shown by using the Wiedemann-Frantz law.

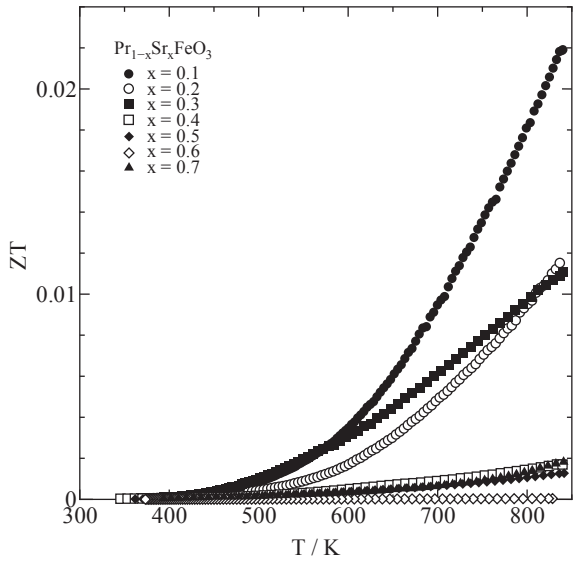

Fig. 14 Temperature dependence of the dimensionless figure of merit (ZT) for $Pr_{1-x}Sr_xFeO_3$ ($0.1 \leq x \leq 0.7$).

scanning electron microscope were carried out using equipment of Yokohama National University Instrumental Analysis and Evaluation Center. Magnetization measurement experiment above room temperature was carried out using the MPMS equipment in the electromagnetic measurement room as a joint use (Approval number: AG68) of the University of Tokyo Physical Institute Laboratory. In addition, the authors would like to express appreciation to Mr. Yoshiki Ishikawa for cooperating in preparing samples for this study.

REFERENCES

1) I. Terasaki, Y. Sasago and K. Uchinokura: Phys. Rev. B **56** (1997) R12685–R12687.
2) Y. Ando, N. Miyamoto, K. Segawa, T. Kawata and I. Terasaki: Phys. Rev. B **60** (1999) 10580–10583.
3) A.C. Masset, C. Michel, A. Maignan, M. Hervien, O. Toulemonde, F. Studer and B. Raveau: Phys. Rev. B **62** (2000) 166–175.
4) Y. Miyazaki, K. Kudo, M. Akoshima, Y. Ono, Y. Koike and T. Kajitani: Jpn. J. Appl. Phys. **39** (2000) L531–L533.
5) P. Boullay, B. Domengès, M. Hervieu, D. Groult and B. Raveau: Chem. Mater. **8** (1996) 1482–1489.
6) S. Hébert, S. Lambert, D. Pelloquin and A. Maignan: Phys. Rev. B **64** (2001) 172101.
7) D. Pelloquin, A. Maignan, S. Hebert, C. Martin, M. Hervieu, C. Michel, L.B. Wang and B. Raveau: Chem. Mater. **14** (2002) 3100–3105.
8) D. Pelloquin, A. Maignan, S. Hebert, C. Martin and B. Raveau: J. Solid State Chem. **170** (2003) 374–381.
9) Y. Miyazaki, T. Miura, Y. Ono and T. Kajitani: Jpn. J. Appl. Phys. **41** (2002) L849–L851.
10) H. Leligny, D. Grebille, O. Pérez, A.-C. Masset, M. Herveieu, C. Michel and B. Raveau: C. R. Acad. Sci., Ser. IIc **2** (1999) 409–414.
11) T. Itoh and I. Terasaki: Jpn. J. Appl. Phys. **39** (2000) 6658–6660.
12) M. Hervieu, A. Maignan, C. Michel, V. Hardy, N. Creon and B. Raveau: Phys. Rev. B **67** (2003) 045112.
13) K. Sakai, M. Karppinen, J.M. Chen, R.S. Liu, S. Sugihara and H. Yamauchi: Appl. Phys. Lett. **88** (2006) 232102.
14) T. Motohashi, Y. Nonaka, K. Sakai, M. Karppinen and H. Yamauchi: J. Appl. Phys. **103** (2008) 033705.
15) M. Ohtaki, T. Tsubota, K. Eguchi and H. Arai: J. Appl. Phys. **79** (1996) 1816–1818.
16) T. Tsubota, M. Ohtaki, K. Eguchi and H. Arai: J. Mater. Chem. **7** (1997) 85–90.
17) T. Tsubota, M. Ohtaki, K. Eguchi and H. Arai: J. Mater. Chem. **8** (1998) 409–412.
18) D. Flahaut, T. Mihara, R. Funahashi, N. Nabeshima, K. Lee, H. Ohta and K. Koumoto: J. Appl. Phys. **100** (2006) 084911.
19) X.Y. Huang, Y. Miyazaki and T. Kajitani: Solid State Commun. **145** (2008) 132–136.
20) S. Urata, R. Funahashi, T. Mihara, A. Kosuga, S. Sodeoka and T. Tanaka: Int. J. Appl. Ceram. Technol. **4** (2007) 535–540.
21) K. Nagasawa, S. Daviero-Minaud, N. Preux, A. Rolle, P. Roussel, H. Nakatsugawa and O. Mentre: Chem. Mater. **21** (2009) 4738–4745.
22) S. Ohta, H. Ohta and K. Koumoto: J. Ceram. Soc. Jpn. **114** (2006) 102–105.
23) M. Ohtaki, H. Koga, T. Tokunaga, K. Eguchi and H. Arai: J. Solid State Chem. **120** (1995) 105–111.
24) M. Iijima and N. Murayama: Proc. Int. Conf. Thermoelectrics. ICT98, (1998) pp. 598–601.
25) K. Iwasaki, T. Ito, T. Nagasaki, Y. Arita, M. Yoshino and T. Matsui: J. Solid State Chem. **181** (2008) 3145–3150.
26) W. Koshibae, K. Tsutsui and S. Maekawa: Phys. Rev. B **62** (2000) 6869–6872.
27) H. Nakatsugawa, M. Kubota and M. Saito: Mater. Trans. **56** (2015) 864–871.
28) H. Nakatsugawa, M. Saito and Y. Okamoto: J. Electron. Mater. **46** (2017) 3262–3272.
29) J.B. MacChesney, R.C. Sherwood and J.F. Potter: J. Chem. Phys. **43** (1965) 1907–1913.
30) T. Takeda, Y. Yamaguchi and H. Watanabe: J. Phys. Soc. Jpn. **33** (1972) 967–969.
31) Y. Takeda, K. Kanno, T. Takeda, O. Yamamoto, M. Takano, N. Nakayama and Y. Bando: J. Solid State Chem. **63** (1986) 237–249.
32) F. Izumi and K. Momma: Solid State Phenom. **130** (2007) 15–20.
33) V.M. Goldschmidt: Naturwissenschaften **14** (1926) 477–485.
34) I.D. Brown: Chem. Rev. **109** (2009) 6858–6919.
35) D. Emin and T. Holstein: Ann. Phys. **53** (1969) 439–520.
36) I.G. Austin and N.F. Mott: Adv. Phys. **18** (1969) 41–102.
37) L. Murawski, C.H. Chung and J.D. Mackenzie: J. Non-Cryst. Solids **32** (1979) 91–104.
38) T.T.M. Palstra, A.P. Ramirez, S.-W. Cheong, B.R. Zegarski, P. Schiffer and J. Zaanen: Phys. Rev. B **56** (1997) 5104–5107.